Supersolid phase of the extended Bose-Hubbard model with an artificial gauge field

K. Suthar [1,2] Hrushikesh Sable [1,3] Rukmani Bai [1,3] Soumik Bandyopadhyay [1,3] Sukla Pal [1,4] and D. Angom [1,*]

[1]*Physical Research Laboratory, Ahmedabad 380009, Gujarat, India*

[2]*Instytut Fizyki imienia Mariana Smoluchowskiego, Uniwersytet Jagielloński, ulica Łojasiewicza 11, 30-348 Kraków, Poland*

[3]*Indian Institute of Technology Gandhinagar, Palaj, Gandhinagar 382355, Gujarat, India*

[4]*Department of Physics, Centre for Quantum Science, and Dodd-Walls Centre for Photonic and Quantum Technologies, University of Otago, Dunedin, New Zealand*

We examine the zero- and finite-temperature phase diagrams of soft-core bosons of the extended Bose-Hubbard model on a square optical lattice. To study various quantum phases and their transitions we employ single-site and cluster Gutzwiller mean-field theory. We have observed that the Mott insulator phase vanishes above a critical value of nearest-neighbor interaction and the supersolid phase occupies a larger region in the phase diagram. We show that the presence of an artificial gauge field enlarges the domain of the supersolid phase. The finite temperature destroys the crystalline structure of the supersolid phase and thereby favors the normal fluid–to–superfluid phase transition. The presence of an envelope harmonic potential demonstrates the coexistence of different phases, and at $zk_BT \geqslant V$, thermal energy comparable to or higher than the long-range interaction energy, the supersolidity of the system is destroyed.

I. INTRODUCTION

Ultracold atomic systems have played an important role in the study of quantum many-body systems. In particular, the novel experimental developments in manipulating ultracold atoms in optical lattices have led to the realization of new quantum states and quantum phase transitions in strongly correlated systems [1,2]. In recent years, there has been a surge of interest in understanding the supersolid (SS) phase, which is characterized by the simultaneous appearance of a crystalline and an off-diagonal long-range order [3,4]. This phase breaks two continuous symmetries: the phase invariance of the superfluid (SF) and translational invariance to form crystal. Although the SS phase was predicted in liquid ^{4}He a long time ago [5,6], the experimental observation of supersolidity in liquid ^{4}He remains elusive [7–9]. However, the quest for the SS phase has gained new impetus following the remarkable theoretical insights and experimental achievements in ultracold atoms in optical lattices, which are excellent quantum many-body systems to observe the SS phase, as they are clean and controllable. Recently, the characteristic signature of the SS phase has been observed in ultracold atoms [10–14] and this phase may emerge by tuning the bosonic interactions of different length scales [15]. Furthermore, the excitation spectrum and various properties of the SS phase have been observed in recent quantum gas experiments [16–18].

Regarding the theoretical aspects, the existence of the SS phase has been studied using the extended Bose-Hubbard model (eBHM). The *checkerboard* supersolid phase of hard-core bosons is thermodynamically unstable towards phase separation and this phase is not stabilized by next-nearest-neighbor (NNN) interactions [19]. However, in the soft-core model, due to the larger Fock space and possibility of a higher number fluctuations, the SS order is stable with nearest-neighbor (NN) interactions [20–22]. Similarly, the SS phase emerges in honeycomb lattices when the hard-core limit of bosons is relaxed [23,24]. The existence and stability of supersolidity have also been confirmed for bosons with infinite-range cavity-mediated interactions [25]. The SS phase has been explored in various lattice systems, such as the one-dimensional chain [26,27] and ladder [28], two-dimensional (2D) square [21,29–34], triangular [35–40], honeycomb [23,24], kagome [41,42], and bilayer lattices of dipolar bosons [43], and three-dimensional cubic lattice [31,44–46]. The eBHM with an artificial gauge field has been studied to examine the fractional quantum Hall [47] and vortex-solid states [48].

In this work we investigate theoretically the presence of the SS phase of soft-core bosons in a 2D square optical lattice with long-range interaction and an artificial gauge field. The long-range interaction can be realized with dipolar ultracold atoms [49,50]. And it is possible to introduce an artificial gauge field with lasers [51–54]. For our studies we use the single-site and cluster mean-field theories. We show that the combined effect of the long-range interaction and artificial gauge field increases the domain of the SS phase. In particular, we examine the effect of magnetic flux quanta on the SS-SF phase boundary in the presence of the NN interaction. Furthermore, to relate to experimental realizations, we incorporate the effects of thermal fluctuations arising from finite temperatures.

The paper is organized as follows. In Sec. II we introduce the model considered in our study and describe the theoretical approach employed. Here we provide a description of the single-site, cluster, and finite-temperature Gutzwiller (GW) mean-field theories. Ground-state phase diagrams and study

*angomd@gmail.com

of dipolar atoms in the confining potential are presented in Sec. III. Finally, we conclude with the key findings of the present work in Sec. IV.

II. THEORETICAL METHODS

A. Extended Bose-Hubbard model

Consider a system of bosonic atoms with long-range interactions in a 2D square optical lattice in the presence of a synthetic magnetic field. The temperature of the system is low so that all the atoms occupy the lowest Bloch band. Such a system is well described by the eBHM, and the Hamiltonian of the model is

$$
\begin{aligned}
\hat{H}_{\text{eBHM}} = & -\sum_{p,q} \left(J_x \hat{b}_{p+1,q}^{\dagger} \hat{b}_{p,q} + J_y \hat{b}_{p,q+1}^{\dagger} \hat{b}_{p,q} + \text{H.c.} \right) \\
& + \sum_{p,q} \hat{n}_{p,q} \left[(\epsilon_{p,q} - \mu) + \frac{U}{2} (\hat{n}_{p,q} - 1) \right] \\
& + \sum_{\langle \xi \xi' \rangle} V_{\xi,\xi'} \, \hat{n}_{\xi} \hat{n}_{\xi'},
\end{aligned} \tag{1}
$$

where $p(q)$ is the lattice site index along the $x(y)$ direction, $\hat{b}_{p,q}^{\dagger}$ ($\hat{b}_{p,q}$) is the bosonic operator which creates (annihilates) an atom at the lattice site (p,q), $\hat{n}_{p,q} = \hat{b}_{p,q}^{\dagger} \hat{b}_{p,q}$ is the boson number operator, J_x and J_y are the tunneling or hopping strength between two NN sites along the x and y directions, respectively, $\epsilon_{p,q}$ is the offset energy arising due to the presence of an external envelope potential, μ is the chemical potential, and $U > 0$ is the on-site interatomic interaction. Here ξ is a combination of lattice indices in two dimensions, that is, $\xi \equiv (p,q)$ and $\xi' \equiv (p',q')$ are neighboring sites to ξ. The long-range interaction $V_{\xi,\xi'}$ is given by

$$
V_{\xi,\xi'} = \begin{cases} V_1 & \text{if } |\mathbf{r}_{pq} - \mathbf{r}_{p'q'}| = a, \\ V_2 & \text{if } |\mathbf{r}_{pq} - \mathbf{r}_{p'q'}| = \sqrt{2}a, \\ 0 & \text{otherwise,} \end{cases} \tag{2}
$$

where a is the lattice spacing, and $\mathbf{r}_{pq} = (pa, qa)$ are the lattice site coordinates. The parameters $V_1 \geqslant 0$ and $V_2 \geqslant 0$ are the NN and NNN interactions, respectively. In the present work, we consider $V_2/V_1 = 1/2\sqrt{2}$, which corresponds to the inverse cube power law of the isotropic dipolar interaction. These terms encapsulate the observable effects of the dipolar interaction in the system. The higher V_1 compared to V_2 tends to induce a checkerboard density pattern for the density wave (DW) and SS phases. This minimal model captures the essential physics arising due to the hopping-induced competition among different solid orders and the superfluidity. We also consider this model to examine the ground states of inhomogeneous dipolar bosons at zero and finite temperatures in optical lattices with an envelope confining harmonic potential.

B. Artificial gauge field

The long-range interaction in the above Hamiltonian, Eq. (1), is characteristic of or inherent to the internal state of the atomic species. In terms of the many-body physics, the nature of the correlation can further be modified through the introduction of an artificial gauge field. The presence of the artificial gauge field modifies the Hamiltonian to

$$
\begin{aligned}
\hat{H}_{\text{eBHM}} = & -\sum_{p,q} \left(J_x e^{i2\pi\alpha q} \hat{b}_{p+1,q}^{\dagger} \hat{b}_{p,q} + J_y \hat{b}_{p,q+1}^{\dagger} \hat{b}_{p,q} + \text{H.c.} \right) \\
& + \sum_{p,q} \hat{n}_{p,q} \left[(\epsilon_{p,q} - \mu) + \frac{U}{2} (\hat{n}_{p,q} - 1) \right] \\
& + \sum_{\langle \xi \xi' \rangle} V_{\xi,\xi'} \, \hat{n}_{\xi} \hat{n}_{\xi'},
\end{aligned} \tag{3}
$$

where the strength of the magnetic field is reflected in the number of flux quanta per plaquette $\alpha = (e/\hbar) \int d\mathbf{r}.\mathbf{A}(\mathbf{r})$. Here, $0 \leqslant \alpha < 1$, and $\mathbf{A}(\mathbf{r})$ is the vector potential which gives rise to the synthetic magnetic field $\mathbf{B} = \nabla \times \mathbf{A}$. In the presence of the synthetic magnetic field, atoms acquire a $2\pi\alpha$ phase when they hop around a plaquette. This results in a phase shift in the hopping strength of the model. Physically, the synthetic magnetic field introduces a force on the atoms which is equivalent to the Lorentz force on a charged particle in the presence of an external magnetic field. The system is then a charge-neutral analog of the quantum Hall system in condensed matter systems. In the present study, we consider the Landau gauge, where the vector potential $\mathbf{A}(\mathbf{r}) = -By\hat{x}$. Hence, for the homogeneous system, at zero magnetic field the system possesses translational invariance along both axes, whereas in the presence of a magnetic field the system preserves the invariance only along the x axis of the lattice.

C. Gutzwiller mean-field theory

To study the ground states of the systems described by the model Hamiltonians in Eqs. (1) and (3) and their properties we use the single-site Gutzwiller mean-field (SGMF) and cluster Gutzwiller mean-field (CGMF) theories. The latter is an extension of the SGMF which incorporates the correlation within a cluster of neighboring sites exactly. In the SGMF theory [34,55–59], the bosonic operators are expanded about their expectation values as

$$
\hat{b}_{p,q} = \phi_{p,q} + \delta\hat{b}_{p,q}, \tag{4a}
$$

$$
\hat{b}_{p,q}^{\dagger} = \phi_{p,q}^{*} + \delta\hat{b}_{p,q}^{\dagger}. \tag{4b}
$$

Therefore, the product of the creation and annihilation operators which occurs in the hopping term can be written as

$$
\hat{b}_{p,q}^{\dagger} \hat{b}_{p',q'} \approx \phi_{p,q}^{*} \hat{b}_{p',q'} + \hat{b}_{p,q}^{\dagger} \phi_{p',q'} - \phi_{p,q}^{*} \phi_{p',q'}, \tag{5}
$$

where second-order terms in the fluctuation $\delta\hat{b}_{p,q}$ are neglected. Here, $\phi_{p,q} = \langle \hat{b}_{p,q} \rangle$ is the SF order parameter of the system. Using the above approximation in the Hamiltonian, Eq. (3), the single-site mean-field Hamiltonian is

$$
\begin{aligned}
\hat{H}_{p,q}^{\text{MF}} = & -\left[J_x e^{i2\pi\alpha q} \left(\phi_{p+1,q}^{*} \hat{b}_{p,q} - \phi_{p+1,q}^{*} \phi_{p,q} \right) \right. \\
& \left. + J_y (\phi_{p,q+1}^{*} \hat{b}_{p,q} - \phi_{p,q+1}^{*} \phi_{p,q}) + \text{H.c.} \right] \\
& + \left[(\epsilon_{p,q} - \mu) + \frac{U}{2} (\hat{n}_{p,q} - 1) \right] \hat{n}_{p,q} \\
& + \sum_{\langle \xi,\xi' \rangle} V_{\xi,\xi'} (\hat{n}_{\xi} \langle \hat{n}_{\xi'} \rangle - \langle \hat{n}_{\xi} \rangle \langle \hat{n}_{\xi'} \rangle),
\end{aligned} \tag{6}
$$

and the total Hamiltonian of the system is

$$\hat{H}_{\mathrm{MF}} = \sum_{p,q} \hat{H}_{p,q}^{\mathrm{MF}}. \qquad (7)$$

Here, the neighboring lattice sites are coupled through $\phi_{p,q}$, the SF order parameter. And therefore the eigenstate of the entire lattice is the product of single-site states. Accordingly, the many-body wave function of the ground state of the system is given by the GW ansatz

$$|\Psi\rangle = \prod_{p,q} |\psi\rangle_{p,q} = \prod_{p,q} \left(\sum_{n=0}^{N_b} c_n^{(p,q)} |n\rangle_{p,q} \right), \qquad (8)$$

where $|\psi\rangle_{p,q}$ is the single-site ground state, N_b is the number of the occupation basis or maximum number of bosons at each lattice site, $|n\rangle_{p,q}$ is the occupation or Fock state of n bosons occupying site (p,q), and $c_n^{(p,q)}$ are the coefficients of the occupation state. The normalization of the wave function leads to the normalization of $c_n^{(p,q)}$ at each lattice site as $\Sigma_n |c_n^{(p,q)}|^2 = 1$. Using the above ansatz the SF order parameter $\phi_{p,q} = \langle\Psi| \hat{b}_{p,q} |\Psi\rangle$ is obtained as

$$\phi_{p,q} = \sum_{n=0}^{N_b} \sqrt{n}\, c_{n-1}^{(p,q)*} c_n^{(p,q)}. \qquad (9)$$

Similarly, the occupancy of each lattice site $n_{p,q} = \langle\Psi| \hat{b}_{p,q}^\dagger \hat{b}_{p,q} |\Psi\rangle$ is

$$n_{p,q} = \sum_{n=0}^{N_b} n |c_n^{(p,q)}|^2. \qquad (10)$$

The two parameters $\phi_{p,q}$ and $n_{p,q}$ together serve to define the quantum phases of the system. Using the mean-field Hamiltonian, Eq. (6), the total energy of the system $E = \langle\Psi| \hat{H}_{\mathrm{MF}} |\Psi\rangle$ is obtained as a sum of the single-site energies $E_{p,q} = \langle\Psi| \hat{H}_{p,q}^{\mathrm{MF}} |\Psi\rangle$. And E is minimized self-consistently with Eqs. (9) and (10) to obtain the ground state of the system.

In the CGMF theory, a lattice of dimension $K \times L$ is partitioned into W clusters of size $M \times N$, that is, $W = (K \times L)/(M \times N)$ [58–64]. Then the hopping terms of the model are decomposed into two types. One is the exact term which corresponds to hopping within the cluster, and the other is the intercluster hopping between lattice sites which lie on the boundary of two neighboring clusters. The latter is defined by coupling through the mean-field or the SF order parameter. The Hamiltonian of a cluster is

$$\hat{H}_C = -\sum_{p,q\in C}{}' \left(J_x e^{i2\pi\alpha q} \hat{b}_{p+1,q}^\dagger \hat{b}_{p,q} + J_y \hat{b}_{p,q+1}^\dagger \hat{b}_{p,q} + \mathrm{H.c.} \right)$$
$$- \sum_{p,q\in\delta C} \left(J_x e^{i2\pi\alpha q} (\phi_{p+1,q}^c)^* \hat{b}_{p,q} + J_y (\phi_{p,q+1}^c)^* \hat{b}_{p,q} + \mathrm{H.c.} \right)$$
$$+ \sum_{p,q\in C} \left[(\epsilon_{p,q} - \mu) \hat{n}_{p,q} + \frac{U}{2} \hat{n}_{p,q}(\hat{n}_{p,q} - 1) \right]$$
$$+ \sum_{\langle\xi\xi'\rangle\in C} V_{\xi,\xi'}\, \hat{n}_\xi\, \hat{n}_{\xi'} + \sum_{\langle\xi\xi'\rangle\in\delta C} V_{\xi,\xi'}\, \hat{n}_\xi\, \langle\hat{n}_{\xi'}\rangle, \qquad (11)$$

where the model parameters J_x, J_y, U, and $V_{\xi,\xi'}$ are defined as in the SGMF and the prime in the first summation indicates

that the $(p+1, q)$ and $(p, q+1)$ lattice sites are also within the cluster. Here, δC in the second summation represents the lattice sites at the boundary of the clusters and $(\phi_{p,q}^c) = \sum_{p',q'\notin C} \langle\hat{b}_{p',q'}\rangle$ is the SF order parameter at the lattice site which lies at the boundary of the neighboring cluster. Like the hopping parameter, the long-range interaction term also has two contributions; one is within the cluster, which is exact, and the other is the intercluster interaction at the boundary, which is defined through the mean occupancy $\langle\hat{n}_{\xi'}\rangle$. The matrix elements of $\hat{H}_C$ are then calculated in terms of the cluster basis states,

$$|\Phi_c\rangle_\ell = \prod_{q=0}^{N-1} \prod_{p=0}^{M-1} |n_p^q\rangle, \qquad (12)$$

where $|n_p^q\rangle$ is the occupation number basis at the (p,q) lattice site, and $\ell \equiv \{n_0^0, n_1^0, \ldots, n_{M-1}^0, n_0^1, n_1^1, \ldots n_{M-1}^1, \ldots, n_{M-1}^{N-1}\}$ is the index quantum number to identify the cluster state. After diagonalizing the Hamiltonian, we can get the ground state of the cluster as

$$|\Psi_c\rangle = \sum_\ell C_\ell |\Phi_c\rangle_\ell, \qquad (13)$$

where C_ℓ are components of the eigenvector and naturally satisfy the normalization condition $\sum_\ell |C_\ell|^2 = 1$. The ground state of the entire $K \times L$ lattice, as in the SGMF, is the direct product of the cluster ground states

$$\left| \Psi_{\mathrm{GW}}^c \right\rangle = \prod_k |\Psi_c\rangle_k, \qquad (14)$$

where k is the cluster index and varies from 1 to $W = (K \times L)/(M \times N)$. The SF order parameter ϕ, as in Eq. (9), can be computed in terms of the cluster states. The average occupancy of the kth cluster can also be computed similarly.

D. Finite-temperature Gutzwiller mean-field theory

At finite temperature, the thermal fluctuations modify the properties of the system, and observable properties are the thermal averages. To calculate the thermal averages we need the entire eigenspectrum. So, in the SGMF, we retain the entire energy spectrum $E_{p,q}^l$ and the eigenstates $|\psi\rangle_{p,q}^l$ obtained from the diagonalization of the single-site Hamiltonian $\hat{H}_{p,q}^{\mathrm{MF}}$ in Eq. (6). Then we evaluate the single-site partition function of the system,

$$Z = \sum_{l=1}^{N_b} e^{-\beta E^l}, \qquad (15)$$

where $\beta = 1/k_B T$ and T is the temperature of the system. At finite T, the region in the phase diagram with $\phi = 0$ and the real occupancy $\langle\hat{n}_{p,q}\rangle$ is identified as the normal fluid (NF) phase. Similarly, in the CGMF, the partition function is defined in terms of all the eigenvalues E_k^l and eigenfunctions $|\Psi_c\rangle_k^l$ of each kth cluster from all the W clusters.

From the definition of the partition function, in the SGMF, the thermal average of $\phi_{p,q}$ is

$$\langle\phi_{p,q}\rangle = \frac{1}{Z} \sum_{i=0}^{N_b} {}_{p,q}^i\langle\psi| \hat{b}_{p,q} e^{-\beta E^i} |\psi\rangle_{p,q}^i, \qquad (16)$$

TABLE I. Classification of phases at zero and finite temperatures.

Quantum phase	$n_{p,q}$	$\phi_{p,q}$	$\langle \Delta n \rangle$	κ
Mott insulator (MI)	Integer	0	0	0
Density wave (DW)	Integer	0	$\neq 0$ (integer)	0
Supersolid (SS)	Real	$\neq 0$	$\neq 0$ (real)	$\neq 0$
Superfluid (SF)	Real	$\neq 0$	0	$\neq 0$
Normal fluid (NF)	Real	0	0 or real	$\neq 0$

where $\langle \ldots \rangle$ represents the thermal averaging. Similarly, the occupancy or the density at finite T is defined as

$$\langle \langle \hat{n}_{p,q} \rangle \rangle = \frac{1}{Z} \sum_{i=0}^{N_b} {}_{p,q}^{i} \langle \psi | \hat{n}_{p,q} e^{-\beta E^i} | \psi \rangle_{p,q}^{i}. \qquad (17)$$

The average occupancy is $\langle n \rangle = \sum_{p,q} \langle \langle \hat{n}_{p,q} \rangle \rangle / (K \times L)$. These definitions can be extended to the CGMF by replacing the single-site states and energies with those of the cluster.

E. Characterization of phases

The ground-state phases in the eBHM and the phase boundaries are characterized by several order parameters. At zero temperature, the ground states of the eBHM support two incompressible and two compressible phases. The incompressible phases are the Mott insulator (MI) and DW and the compressible phases are the SS and SF. Among these phases, the DW and SS are due to the long-range interaction between atoms. The characteristic distinction between the DW and the MI is their density distributions: the MI has commensurate occupancy, whereas the DW phase has incommensurate occupancy with long-range crystalline order. The insulating phases have zero ϕ and integer occupancy of each site $n_{p,q}$; on the other hand, the compressible phases have finite ϕ and real $n_{p,q}$. We identify the phase boundaries between the MI(DW) and the SF(SS) phases based on the order parameter ϕ and $n_{p,q}$. The SS phase has long-range crystalline order in ϕ and $n_{p,q}$, whereas the SF phase has a uniform density distribution of atoms. The DW and SS phases are better described in terms of sublattices A and B such that the NN sites belong to different sublattices. The relative average occupancy $\langle \Delta n \rangle$ is another order parameter which can distinguish the DW and SS phases from the MI and SF phases. In the SGMF method, for a $K \times L$ lattice it is defined as

$$\langle \Delta n \rangle = \frac{1}{K \times L} \sum_{\langle \xi \xi' \rangle} |\langle \hat{n}_\xi \rangle - \langle \hat{n}_{\xi'} \rangle|, \qquad (18)$$

where $\langle \hat{n}_\xi \rangle \equiv \langle \hat{n}_A \rangle$ and $\langle \hat{n}_{\xi'} \rangle \equiv \langle \hat{n}_B \rangle$ are sublattice occupancies. A similar expression can be defined for the CGMF theory. For the DW and SS phases $\langle \Delta n \rangle$ is nonzero, and in particular, it is integer and real for the DW and SS phases, respectively. But for the MI and SF phases $\langle \Delta n \rangle$ is zero, as $\langle \hat{n}_{p,q} \rangle$ is uniform. Table I summarizes the classification of all the phases discussed in the present work.

At finite temperature, an NF phase is present in the system which is distinguishable from the incompressible MI and DW phases by examining the local density variance, which is also

the measure of the local compressibility [65,66]

$$\kappa = \frac{\partial \langle \hat{n} \rangle}{\partial \mu} = \beta \left(\langle \hat{n}_{p,q}^2 \rangle - \langle \hat{n}_{p,q} \rangle^2 \right). \qquad (19)$$

This quantity defines the density fluctuations of the system. κ is zero for MI and DW phases whereas it is nonzero for the NF phase. We use these order parameters to obtain the phase boundaries between various phases at zero and finite temperatures. In the phase diagrams, discussed in the next section, the incompressible phases are indicated by their sublattice occupancies (n_A, n_B), with $n_A = n_B$ for the MI and $n_A \neq n_B$ for the DW phase.

III. RESULTS AND DISCUSSION

The standard BHM shows two phases, the incompressible MI phase, corresponding to commensurate integer filling, and the compressible SF phase, which has finite ϕ. The SF-MI quantum phase transition was observed by tuning the depth of the optical lattice [67]. In the eBHM, the introduction of the NN interaction changes the phase diagram through the emergence of two more phases. First is the DW, which sandwiches the MI lobes at low values of NN interaction, and second is the SS phase, which occurs as an envelope around the DW lobes. In this work, we first examine the phase diagram for homogeneous systems. We then study the impact of an artificial gauge field on the phase diagram by considering $\alpha = 1/2$. For comparison with experimental realizations, we also study this with an envelope potential.

A. Homogeneous case

The phase diagram of the eBHM obtained from the SGMF is as shown in Fig. 1 for different values of V. It is important to note that here V is the NN interaction which is V_1 of long-range interaction [Eq. (2)] and $V_2 = 0$. In the phase diagram, the incompressible DW and MI phases are identified by their sublattice occupancies (n_A, n_B). We observed that for $zV < U$, where z is the coordination number of the system, the ground state alternates between MI and DW phases, and regions of the SS phase occur as envelopes around the DW phase lobes. With increasing V, at a critical value $zV_c = U$ the MI lobes are transformed into the DW phase. For $V \geqslant V_c$, the SS phase occupies a larger region in the phase diagram. As V is increased, the other observable effect is that the critical value of the hopping strength J_c/U for the DW-SS transition also increases. At higher values, when $zV \gtrsim 1.5U$, the SS-SF phase boundary is like a linear function of J, and this is discernible in Fig. 1(d). In particular, the phase boundary is linear when $zJ/U > 1$. These findings are in good agreement with the previous work of Iskin [68]. The numerical results of the phase boundaries are in good agreement with the analytical predictions of mean-field decoupling theory [69]. For example, the critical hopping J_c/U for the DW(1,0)-to-SS transition at $V/U = 0.32$ is 0.0994 and analytical theory predicts the same value for this set of parameters. Similarly, we find that the MI-SF phase boundaries from our study are consistent with the mean-field decoupling theory [69]. To examine the importance of the intersite correlation effects the phase diagram using the 2×2 CGMF method is as shown
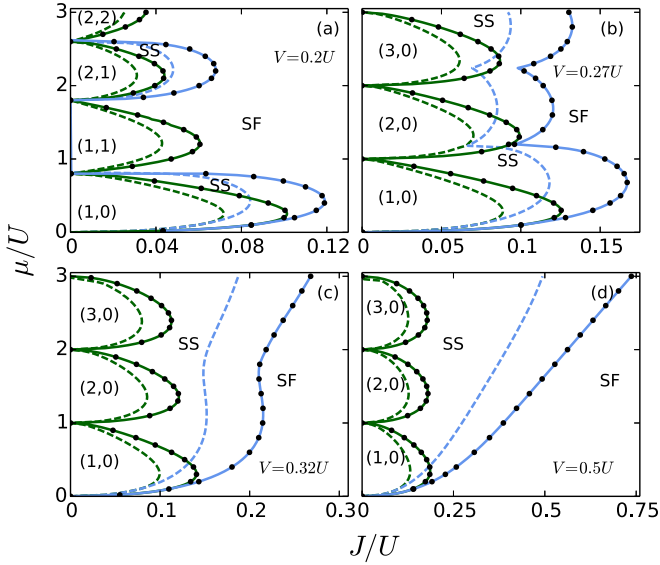
FIG. 1. Phase diagrams of the eBHM with uniform hopping amplitude ($J_x = J_y = J$) for (a) $V/U = 0.2$, (b) $V/U = 0.27$, (c) $V/U = 0.32$, and (d) $V/U = 0.5$. Plots show the phase boundaries for two cases, $\alpha = 0$ and $\alpha = 1/2$. The dashed (solid) green line indicates the MI-SF, DW-SF, and DW-SS phase boundaries for the $\alpha = 0$ ($\alpha = 1/2$) case. The dashed (solid) blue line represents the SS-SF phase boundary for the $\alpha = 0$ ($\alpha = 1/2$) case. The phase boundaries in the $\alpha = 1/2$ case are obtained using the Landau gauge. Data points obtained using the symmetric gauge are represented by filled black circles. Here, the DW and MI phases are indicated by their sublattice occupancies (n_A, n_B).

FIG. 2. Phase diagrams of the eBHM obtained from the CGMF theory with 2×2 clusters for a uniform hopping amplitude ($J_x = J_y = J$) at (a) $V/U = 0.2$, (b) $V/U = 0.27$, (c) $V/U = 0.32$, and (d) $V/U = 0.5$. Plots show the phase boundaries for two cases, $\alpha = 0$ and $\alpha = 1/2$. The left dashed (solid) green line indicates the MI-SF, DW-SF, and DW-SS phase boundaries for the $\alpha = 0$ ($\alpha = 1/2$) case. The right dashed (solid) blue line represents the SS-SF phase boundary for the $\alpha = 0$ ($\alpha = 1/2$) case. Here the DW and MI phases are indicated by their sublattice occupancies (n_A, n_B).

in Fig. 2. It is qualitatively similar to the one based on the SGMF in Fig. 1. But there are several quantitative differences. First, the MI phase lobe is enhanced, whereas the DW phase lobe is suppressed. As an example, for $V/U = 0.2$ the tip of the DW(1,0) lobe is at $J_c/U = 0.0717$ using SGMF theory, but with CGMF theory it is decreased to 0.0709. Although the difference between the J_c values using the two theories is very small, using higher clusters with the CGMF one can get significantly different J_c's. This is apparent from the cluster finite-size scaling of the cluster sizes discussed in the next subsection. Second, at higher values of V and $\alpha = 1/2$, the SS-SF phase boundary commences at $J/U \approx 0$ and $\mu/U \approx 0$ with the SGMF theory. On the other hand, with the CGMF theory the SS-SF boundary starts at a finite value of J/U and $\mu/U = 0$ [Figs. 2(c) and 2(d)]. Third, compared to the SGMF results, with the CGMF theory we obtain SS domains which are smaller in size. This is due to the better representation of fluctuations in the CGMF theory. Our results demonstrate the greater accuracy of the CGMF theory by correcting the overestimation of the SS domain obtained from the single-site mean-field theory. This observation is also consistent with a similar comparison between results obtained from the single-site mean-field theory and the quantum Monte Carlo (QMC) [22,25]. And, finally, for higher values of V/U the SS-SF boundary is linear at higher μ with the SGMF theory. But it is curved with the CGMF theory. Qualitatively, the value of J_c obtained using the SGMF and CGMF are close to the QMC results available in the literature. The values of J_c/U for the
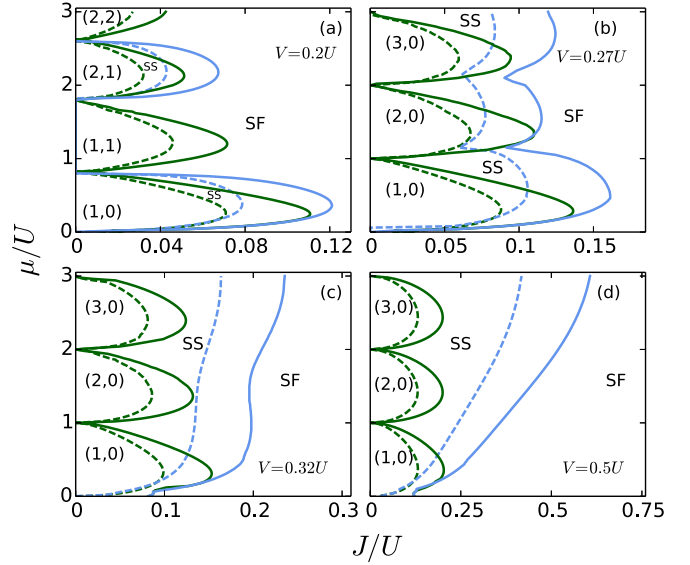
DW(1,0)-SS quantum phase transition at $zV/U = 1$ obtained using the SGMF and CGMF methods are 0.0841 and 0.0832, respectively, and these values are close to the QMC result of 0.0822 [22]. Furthermore, we also carried out additional computations to compare the J_c/U of the DW-SF quantum phase transition at half-filling with the QMC predictions [70]. For example, at $V/U \approx 0.35$, using the SGMF we obtain $J_c/U = 0.175$. Using CGMF theory this value is improved to 0.153. And this is in very good agreement with the QMC result of 0.143 reported in Ref. [70]. Further improvements in the values of the J_c of various quantum phase transitions is possible when clusters of larger sizes are considered. This is also evident from the cluster finite-size scaling analysis discussed in the next subsection.

As mentioned earlier, to study the effect of an artificial gauge field, we choose $\alpha = 1/2$. So, hereafter by *with an artificial gauge field* we mean $\alpha = 1/2$. And *without an artificial gauge field* means $\alpha = 0$. The artificial gauge field modifies the phase boundaries of the MI, DW, and SS phases, and the changes are discernible from the phase diagrams in Fig. 1. For example, for the (1,0) DW lobe at $V/U = 0.2$, the tip of the lobe is enhanced by 40%, from $J_c/U \approx 0.0717$ to $J_c/U \approx 0.101$ with an artificial gauge field. This enhancement of the insulating lobe and the phase boundaries of the DW(MI)-SS(SF) transition with an artificial gauge field is in agreement with the mean-field decoupling theory [69]. For example, the J_c/U of the DW(1,0)-SS quantum phase transition with $\alpha = 1/2$ at $V/U = 0.32$ is 0.1406, which is the same as the value obtained from the analytical theory [69]. The tip of the SS lobe is enhanced from $J_c/U \approx 0.084$ to $J_c/U \approx 0.119$, and

these changes together imply a larger domain of the SS phase surrounding the DW(1,0) phase. These changes arise from the localizing effect of the Landau quantization, associated with the artificial gauge field, on the itinerant bosons. In addition, there are major differences between the SGMF and the CGMF phase diagrams. For example, the tip of the DW(1,0) lobe is increased from $J_c/U \approx 0.101$ in the SGMF to $J_c/U = 0.110$ in the CGMF. This implies that the effect of correlation due to finite magnetic flux is better captured by the CGMF method. We perform a stability analysis of the SS phase by computing the average occupancy $\langle n \rangle$ as a function of μ [21,25]. The unstable phase is characterized by a discontinuity in $\langle n \rangle$ as μ is varied. In our study, we fix the J/U and vary μ/U such that the SS phase is traversed, then compute the average occupancy. As an example, at $J/U = 0.12$ and $V/U = 0.32$ for the $\alpha = 0$ case, we do not observe any discontinuity in $\langle n \rangle$ as a function of μ/U. This confirms the stability of the SS phase of soft-core bosons. We further include the NNN interaction term and find that the SS phase remains stable. The stability of the soft-core SS phase is consistent with the QMC results in Refs. [21] and [22]. In addition, our analysis also demonstrates the stability of the SS phase in the presence of an artificial gauge field.

To check the gauge invariance of the phase boundaries, we also compute the phase boundaries for $\alpha \neq 0$ using the SGMF and CGMF with a symmetric gauge. For the symmetric gauge, the vector potential $\mathbf{A}(\mathbf{r}) = (1/2)(-By\hat{x} + Bx\hat{y})$. We observe that the phase boundaries obtained with the symmetric gauge are in good agreement with the results with the Landau gauge. This can be seen in Fig. 1, where the filled black circles are the phase boundaries obtained using the symmetric gauge. For example, with the symmetric gauge, the tip of the DW(1,0) lobe for $V/U = 0.2$ is $J_c/U = 0.101$, which is identical to the Landau gauge result. Similarly, for the same value of V/U, the CGMF result with 2×2 is $J_c/U = 0.110$. And this result is invariant under Landau and symmetric gauges. The SS-SF phase boundaries are also gauge invariant. To illustrate, consider the SS-SF phase transition for $V/U = 0.2$. With $\mu/U = 0.44$, both the symmetric and the Landau gauges give $J_c/U = 0.119$. And in the case of the CGMF, the value $J_c/U = 0.1207$ obtained with 2×2 clusters is gauge invariant. Thus, the SGMF and CGMF methods give gauge-invariant phase boundaries for the incompressible-to-compressible and SS-SF quantum phase transitions. This is consistent with the general principle that the observable quantities are gauge invariant [71,72]. And it shows that the numerical methods we have used are robust, as the results are gauge invariant.

The nature of the DW-SS transition is better represented by $\langle \Delta n \rangle$ and values for $V = 0.22U$ and $0.32U$ corresponding to $V < V_c$ and $V > V_c$ are shown in Fig. 3. In the figure, the black regions correspond to MI and SF phases and the regions in other colors correspond to DW and SS phases. For $V = 0.22U$, the yellow regions are DW phases and the regions in other shades correspond to SS phases. The gradient of the shades indicates that the transition from DW to SS in terms of $\langle \Delta n \rangle$ is smooth. For the case of $V = 0.32U$, there are no black regions in the neighborhood of $J/U \approx 0$. This is due to the absence of MI lobes and is consistent with the phase diagram shown in Fig. 1, as all the MI lobes are transformed to DW lobes. The nature of the DW phases is apparent and
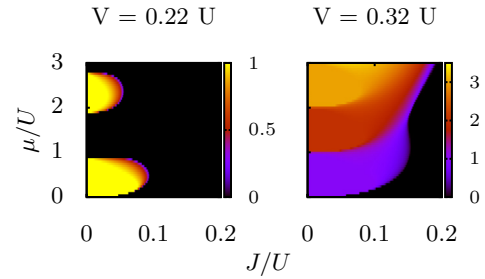

FIG. 3. The relative average occupancy of two consecutive sites are shown as a function of the chemical potential μ and hopping parameter J. The NN interaction is shown at the top.

visible from the color gradient in Fig. 3, as the colors indicate the difference in the occupancy of two neighboring lattice sites. As in the case of $V = 0.22U$, regions with a color gradient indicate the SS phase, and overall the relative average occupancy is in agreement with the phase diagram in Fig. 1. However, the phase diagram in terms of $\langle \Delta n \rangle$ provides a richer description of the two phases, DW and SS, unique to the eBHM vis-à-vis the BHM, and it serves as an appropriate order parameter to examine the regions of the SS phase.

B. Cluster finite-size scaling

The results obtained from the SGMF and CGMF do provide qualitatively correct phase diagrams. And this can be improved further by using a cluster finite-size scaling analysis. Such an analysis provides the location of the phase boundary in the thermodynamic limit. As a case study, we examine the location of the DW and MI lobe tips J_c for $\alpha = 0$, and $V = 0.2U$. To implement the cluster finite-size scaling analysis, we use a series of square and rectangular clusters $N_C = 2 \times 2$, 4×2, 6×2, and 4×4. In addition, we include the results of 4×2 and 4×4 clusters with exact hopping along one spatial direction. Here, we consider clusters with an even number of sites along x and y directions, as only these clusters generate a checkerboard order. To obtain the thermodynamic limit, we introduce the scaling parameter $\lambda = N_B/(N_B + N_{\delta B})$, which varies from 0 to 1. Here, N_B is the number of bonds within the cluster and $N_{\delta B}$ is the number of bonds at the boundary which couple the cluster to its neighbors through the mean-field term [64,73]. The parameter λ is a measure of the atomic correlations taken into account by using clusters of various sizes. In the extreme limits, the SGMF $N_C = 1 \times 1$ and exact $N_C = \infty$ results correspond to $\lambda = 0$ and $\lambda = 1$, respectively. Thus, the value of J_c improves as λ of the cluster approaches 1.

The cluster finite-size scaling analysis for the DW(1,0) and MI(1,1) phases with $\alpha = 0$ and $V = 0.2U$ are shown in Fig. 4. As shown in the figure, the location of the MI lobe tip, J_c, increases with the cluster size. The SGMF favors the SF phase, leading to underestimation of the MI phase. And the CGMF with larger cluster sizes enhances the MI lobe. Based on the linear fit the thermodynamic limit of J_c is 0.05428. One key feature is that the results from the periodic boundary condition with exact hopping in one direction lie closer to the fitted line. And, more importantly, these have higher λ values, as they have fewer bonds coupled to the mean field. The
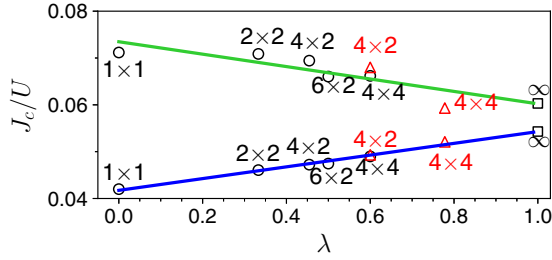
FIG. 4. The cluster finite-size scaling of J_c for the MI(1,1)-SF (blue line) and DW(1,0)-SS (green line) transitions for different cluster sizes. Circles represent the critical values obtained using periodic boundary conditions along bothspatial dimensions; triangles, along one dimension. Squares represent the exact values in the thermodynamic limit. The scaling is performed for $\alpha = 0$ and $V = 0.2U$.

scaling behavior of J_c is in good agreement with the scaling results for MI-SF in the BHM [63,64].

In the case of the DW(1,0) phase, J_c decreases with increasing cluster size. In other words, the domain with DW order decreases with larger clusters and implies that SGMF theory overestimates the DW order. This is corrected by the fluctuations incorporated with larger clusters. The trend is opposite to the MI-phase case. From the cluster finite-size scaling analysis, the linear fit gives the thermodynamic limit of J_c as 0.06021. This trend of J_c is also reported in earlier studies of the hard-core eBHM [40,73]. Furthermore, the scaled J_c values of eBHM phase boundaries at $zV/U = 1$ are in good agreement with the QMC results [22]. In the presence of an artificial gauge field, the qualitative features of the scaling analysis will be modified, and the predicted exact critical values of the transitions will differ from those in the $\alpha = 0$ case.

C. Finite-temperature effects

Thermal fluctuations associated with finite temperatures are an essential feature of experimental observations. Although the zero-temperature phase diagrams do provide key insights and qualitative understanding, to relate them to the experimental results it is essential to incorporate thermal fluctuations. We do this through the approach outlined in Sec. II D. As mentioned earlier, the SS phase is yet to be observed in the eBHM and this could be due to the sensitivity of the phase to thermal fluctuations. At zero temperature, the SS phase appears in the system at a finite value of the NN interaction V. In Fig. 5, we show the finite-temperature phase diagrams obtained using 2×2 clusters in the CGMF method. As we and others have demonstrated [58–64] that the results with the CGMF are more reliable, hereafter we only consider the results from CGMF theory. In the plots in Fig. 5, a distinguishing feature of the thermal fluctuations is the emergence of the NF phase. The thermal fluctuation melts both the MI and the DW phases and destroys the SF phase at the MI-DW and DW-DW boundaries.

To be more specific, at $k_BT = 0.02U$, as shown in Figs. 5(a) and 5(b), the orange shading marks the DW and MI phases and the NF phase exists outside of these. The MI and
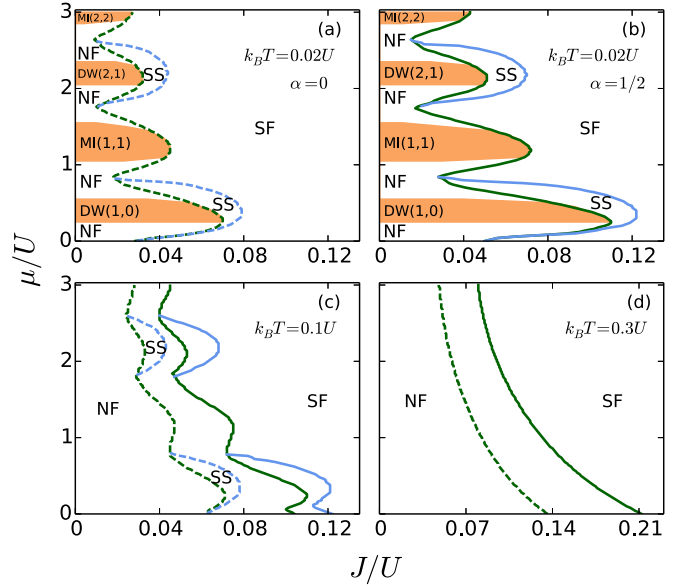

FIG. 5. Finite-temperature phase diagrams of the eBHM obtained from CGMF theory with 2×2 clusters. The shaded orange regions mark the DW and MI phases. (a) Phase diagram for $\alpha = 0$ at $k_BT = 0.02U$. The dashed green line represents the MI-SF, NF-SF, DW-SS, and NF-SS phase boundaries; the dashed blue line, the SS-SF phase boundary. (b) Phase diagram for $\alpha = 1/2$ at $k_BT = 0.02U$. The solid green line marks the MI-SF, NF-SF, DW-SS, and NF-SS phase boundaries; the solid blue line, the SS-SF phase boundary. Phase diagrams for $\alpha = 0$ and $1/2$ at (c) $k_BT = 0.1U$ and (d) $k_BT = 0.3U$, with the combined color scheme from (a) and (b). Here, the NN interaction $V = 0.2U$.

NF phases both have zero ϕ and commensurate densities. The difference is that the MI phase has an integer commensurate density, but the NF phase has a real commensurate density. The DW phase, on the other hand, has a checkerboard density but with integer values. The NF region around the DW phase has an incommensurate real density. By observing the local density variance or the compressibility, the incompressible DW and MI phases can be differentiated from the NF phase as mentioned in Sec. II E. Comparing the plots in Fig. 5(a) and Fig. 5(b), it is clear that the larger MI and DW lobes with a finite α are retained at finite temperatures and hence the larger SS domain as well. At intermediate temperatures, both the MI and the DW phases are entirely transformed into the NF phase but a portion of the SS lobes survives. This is visible in the phase diagram at $k_BT = 0.1U$ shown in Fig. 5(c). In the plots in the figure, the quantitative differences with and without an artificial gauge field are also visible. With an artificial gauge field, the domains of the NF and SS phases are larger. For example, at $\mu = 0$ the NF extends up to $J/U = 0.064$ and $J/U = 0.104$ for zero and finite α, respectively. This trend of a larger extent of the NF phase with finite α extends to higher values of μ. Upon a further increase in temperature the crystalline order of the SS phase is destroyed and it vanishes from the phase diagram. At $k_BT \approx 0.3U$, as shown in Fig. 5(d), only the NF and SF phases are present in the system. At $\mu/U = 0$ the NF-SF phase boundary is located at $J/U = 0.136$ and $J/U = 0.212$ for zero and finite α, respectively.

The separation between the location of the phase boundaries is reduced as μ/U is increased. This is to be expected, as the size of the DW lobes decreases with increasing μ/U. As in the zero-temperature case, the phase boundaries of the finite-temperature phase diagrams are also gauge invariant. We confirmed this by analyzing the phase boundaries using a symmetric gauge. As an illustration, consider the DW-SS transition at $\mu/U = 0.4$ and $k_B T/U = 0.02$ with $\alpha = 1/2$; this point is chosen from the phase diagram in Fig. 5(b). We obtain $J_c/U = 0.098$ using the symmetric gauge and this value is in excellent agreement with the Landau gauge result. Similarly, for the same value of μ/U the SS-SF transition occurs at $J_c/U = 0.122$ and this value is gauge independent. At a higher temperature, $k_B T/U = 0.3$, the phase boundary of the NF-SF transition is also gauge invariant. Hence, comparison of the J_c/U values for various quantum phase transitions using Landau and symmetric gauges demonstrates the gauge invariance of the phase boundaries obtained with the numerical methods we have adopted in this work.

D. Inhomogeneous case

The system considered so far is uniform and we emulate it with a 12×12 lattice with periodic boundary conditions. However, in most quantum gas experiments the optical lattice has a confining envelope potential. Most often the external envelope potential is a harmonic oscillator. Hence, the inhomogeneity arising from this confining potential is another factor to be considered for comparison with the experimental observations. Therefore, we examine the ground state of the eBHM in a 50×50 square lattice with SGMF theory where the external harmonic potential is incorporated in the chemical potential through the offset energy $\epsilon_{p,q} = \Omega(p^2 + q^2)$. Here Ω is the strength of the confining potential. The parameters of the system considered are $J/V = 0.1$, $\mu/V = 2.8$, and $\Omega/V = 0.01$ [74]. The value of Ω is such that the atomic density outside the lattice potential is zero. The finite Ω modifies the local μ and therefore the ground state exhibits coexistence of various phases. Here V is the strength of the dipolar interaction and the range of the potential is considered up to second nearest neighbors. Therefore, for the long-range interaction, Eq. (2), $V_1 = V$ and $V_2 = V/2\sqrt{2}$.

To determine the changes in the competing phases we examine the ground state of the system at $V/U = 0.05, 0.5$, and 1.0. These values cover the weak and strong limits of the dipolar interaction. In the experiments these regimes are reachable using Feshbach resonance in dipolar atoms like Cr [75], Er [76], and Dy [77,78]. As in the previous cases, to study the effects of thermal fluctuations we consider three values of $k_B T/V$: 0, 0.2, and 0.3. At zero temperature, the profiles of $n_{p,q}$ and $\phi_{p,q}$ corresponding to $V/U = 0.05, 0.5$, and 1.0 are shown in Fig. 6. For a weak dipolar interaction $V/U = 0.05$ the density is nearly uniform in the central region. The corresponding $\phi_{p,q}$, though nearly uniform, shows a dip around the center. But it is more uniform at the intermediate strength of the dipole interaction $0.5U$. In both of these cases, $V/U = 0.05$ and 0.5, the central SF region is surrounded by the DW(1,0) phase and this is evident from the ring-shaped profile of the checkerboard density pattern in the figure. The other key feature is that the domain of the DW
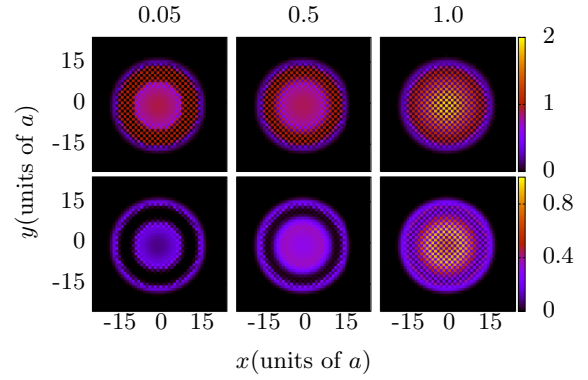

FIG. 6. Zero-temperature density distribution (upper panel) and SF order parameter (lower panel) of a 50×50 square lattice for different values of the dipolar interaction strength V/U. The V/U value is shown at the top. Here x and y are in units of the lattice spacing a.

phase becomes narrower as V/U is increased, and above a critical value $V/U = 0.8$ there is a quantum phase transition from the DW phase to the SS phase. This happens when both the interaction strengths, on-site and dipole interactions, are comparable. As shown in Fig. 6, for $V/U = 1$, there is a large region around the center where both the density and the SF order parameter show checkerboard distributions. This is the signature of the SS phase.

Next, to relate to the experimental realizations we incorporate the finite-temperature effects. For weak dipolar interaction thermal fluctuations lead to the melting of the SF phase. This is evident from the density and SF order parameter corresponding to $V/U = 0.05$ at $k_B T/V = 0.2$ as shown in Fig. 7. A more detailed study, where V/U is fixed and the temperature is changed, shows that the SF phase in the central region does exist at lower temperatures. But it melts to the NF phase at the critical temperature of $k_B T/V = 0.16$. At the higher value of $V/U = 0.5$ the central SF region reemerges and so does the SS phase at the still higher value of $V/U = 1$. In short, with thermal fluctuations it is essential to have stronger dipolar interactions to observe the SS phase. Considering the parameters for the experimental realization
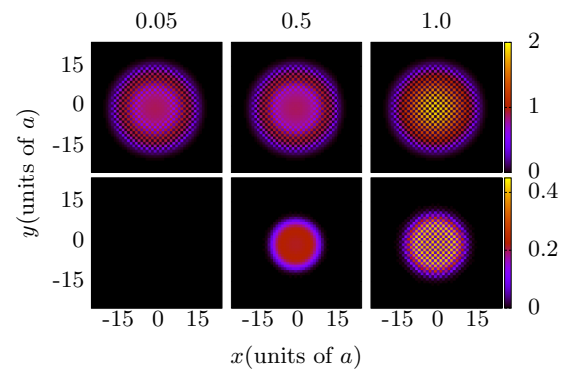

FIG. 7. Density distribution (upper panel) and SF order parameter (lower panel) of a 50×50 square lattice at $k_B T/V = 0.2$ for different values of the dipolar strength V/U. The V/U value is shown at the top. Here x and y are in units of the lattice spacing a.
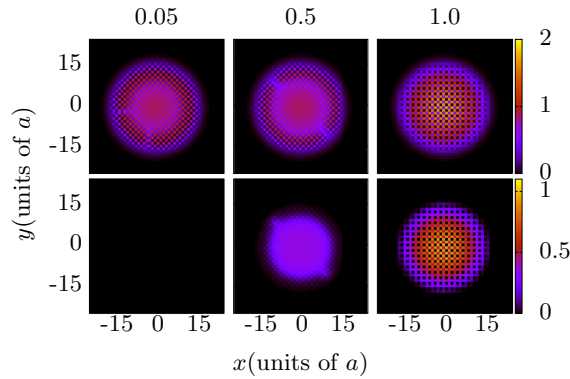
FIG. 8. Density distribution (upper panel) and SF order parameter (lower panel) of a 50×50 square lattice in the presence of an artificial gauge field $\alpha = 1/2$ at $k_B T/V = 0.2$. The V/U value is shown at the top. Here x and y are in units of the lattice spacing a.

of dipolar condensates of ^{168}Er in optical lattices [50], the corresponding temperature of $k_B T/V = 0.2$ is ≈ 40 nK. This is within the experimental realm, and hence the combined effect of the dipolar interaction and artificial gauge field can lead to the emergence of the SS phase within an experimentally achievable parameter domain.

At a higher temperature, $k_B T/V \approx 0.3$, the central region is in the NF phase for weaker dipole interactions $V/U \leqslant 0.5$. Then, upon increasing V/U further the density assumes a checkerboard pattern, but the SF order parameter is zero. That is, the central region of the system is in the DW phase. This is to be compared and contrasted with the earlier result at $k_B T/V \approx 0.2$, where, as shown in Fig. 7 the SS phase exists for $V/U = 1$. Thus, focusing on the strong-interaction domain $V/U = 1$, our results show the existence of an SS-DW transition at $z\, k_B T = V$. In short, the SS phase exists in the system at lower temperatures, but the SS order melts into the DW phase when $z k_B T \geqslant V$. Upon increasing the temperature further, the crystalline structure or diagonal long-range order of the DW phase starts to melt and at $z k_B T \approx 3V$ the system is fully in the NF phase. So, the melting of the SS phase occurs in two steps. First, the off-diagonal long-range SF order is destroyed. This transforms the SS phase into the DW phase. And second, the DW phase melts into the NF phase. In the presence of an artificial gauge field the ground state and the corresponding SF order parameter at $k_B T/V = 0.2$ are shown

in Fig. 8. As in the case of a uniform system, there are no qualitative changes in the results with the introduction of an artificial gauge field, although the atoms have a velocity current. For the parameters considered, at $\mu/V = 2.8$ and $k_B T/V = 0.2$, the SS phase appears in the range $\Delta J = 0.04$, whereas in the presence of a gauge field this range is enhanced to $\Delta J = 0.07$. As discussed in the homogeneous case, for a given μ the range of J values for the SS phase to occur is larger than without a gauge field. This would enhance the possibility of observing the SS phase with the eBHM in experimental realizations.

IV. CONCLUSIONS

We have examined the zero- and finite-temperature phase diagrams of the eBHM in two dimensions using SGMF and CGMF theory. In the presence of an artificial gauge field the domain of the SS phase is enhanced and 2×2 CGMF theory provides a better description of the system. The cluster finite-size scaling analysis demonstrates the key role of fluctuations in determining the quantum phases. For the DW-SS transition, the suppression of fluctuations favors the DW phase. But in the MI-SF transition, suppression of fluctuations favors the SF phase. This is indicated by the decrease and increase in J_c in the DW-SS and MI-SF transitions, respectively. At higher temperatures, thermal fluctuations destroy the SS phase and the phase diagram exhibits an NF-SF transition. Furthermore, we have studied the system of ultracold bosons with long-range interactions in the presence of a harmonic confinement to relate to quantum gas experiments. Our results show that beyond a critical threshold of temperature, $z k_B T \geqslant V$, the SS phase vanishes and the system is occupied by the DW phase. These results suggest that the prospect of observing the SS phase is higher when the temperature $z k_B T < V$; this range of temperatures is possible in experiments on dipolar Bose gases loaded into optical lattices. This offers the opportunity to observe the SS phase with the eBHM in quantum dipolar gas experiments.

[1] M. Lewenstein, A. Sanpera, V. Ahufinger, B. Damski, A. Sen(De), and U. Sen, Ultracold atomic gases in optical lattices: Mimicking condensed matter physics and beyond, Adv. Phys. **56**, 243 (2007).

[2] I. Bloch, J. Dalibard, and W. Zwerger, Many-body physics with ultracold gases, Rev. Mod. Phys. **80**, 885 (2008).

[3] A. J. Leggett, Can a Solid be Superfluid? Phys. Rev. Lett. **25**, 1543 (1970).

[4] G. V. Chester, Speculations on Bose-Einstein condensation and quantum crystals, Phys. Rev. A **2**, 256 (1970).

[5] A. F. Andreev and I. M. Lifshitz, Quantum theory of defects in crystals, Sov. Phys. JETP **29**, 1107 (1969).

[6] D. J. Thouless, The flow of a dense superfluid, Ann. Phys. **52**, 403 (1969).

[7] E. Kim and M. H. W. Chan, Probable observation of a supersolid helium phase, Nature (London) **427**, 225 (2004).

[8] E. Kim and M. H. W. Chan, Observation of superflow in solid helium, Science **305**, 1941 (2004).

[9] D. Y. Kim and M. H. W. Chan, Absence of Supersolidity in Solid Helium in Porous Vycor Glass, Phys. Rev. Lett. **109**, 155301 (2012).

[10] J. Lonard, A. Morales, P. Zupancic, T. Esslinger, and T. Donner, Supersolid formation in a quantum gas breaking a continuous translational symmetry, Nature (London) **543**, 87 (2017).

[11] J.-R. Li, J. Lee, W. Huang, S. Burchesky, B. Shteynas, F. Top, A. O. Jamison, and W. Ketterle, A stripe phase with supersolid properties in spin-orbit-coupled Bose-Einstein condensates, Nature (London) **543**, 91 (2017).

[12] L. Tanzi, E. Lucioni, F. Famà, J. Catani, A. Fioretti, C. Gabbanini, R. N. Bisset, L. Santos, and G. Modugno, Observation of a Dipolar Quantum Gas with Metastable Supersolid Properties, Phys. Rev. Lett. **122**, 130405 (2019).

[13] F. Böttcher, J.-N. Schmidt, M. Wenzel, J. Hertkorn, M. Guo, T. Langen, and T. Pfau, Transient Supersolid Properties in an Array of Dipolar Quantum Droplets, Phys. Rev. X **9**, 011051 (2019).

[14] L. Chomaz, D. Petter, P. Ilzhöfer, G. Natale, A. Trautmann, C. Politi, G. Durastante, R. M. W. van Bijnen, A. Patscheider, M. Sohmen, M. J. Mark, and F. Ferlaino, Long-Lived and Transient Supersolid Behaviors in Dipolar Quantum Gases, Phys. Rev. X **9**, 021012 (2019).

[15] R. Landig, L. Hruby, N. Dogra, M. Landini, R. Mottl, T. Donner, and T. Esslinger, Quantum phases from competing short- and long-range interactions in an optical lattice, Nature (London) **532**, 476 (2016).

[16] G. Natale, R. M. W. van Bijnen, A. Patscheider, D. Petter, M. J. Mark, L. Chomaz, and F. Ferlaino, Excitation Spectrum of a Trapped Dipolar Supersolid and its Experimental Evidence, Phys. Rev. Lett. **123**, 050402 (2019).

[17] L. Tanzi, S. M. Roccuzzo, E. Lucioni, F. FamÃ, A. Fioretti, C. Gabbanini, G. Modugno, A. Recati, and S. Stringari, Supersolid symmetry breaking from compressional oscillations in a dipolar quantum gas, Nature **574**, 382 (2019).

[18] M. Guo, F. Böttcher, J. Hertkorn, J.-N. Schmidt, M. Wenzel, H. P. Büchler, T. Langen, and T. Pfau, The low-energy goldstone mode in a trapped dipolar supersolid, Nature **574**, 386 (2019).

[19] G. G. Batrouni and R. T. Scalettar, Phase Separation in Supersolids, Phys. Rev. Lett. **84**, 1599 (2000).

[20] A. van Otterlo, K.-H. Wagenblast, R. Baltin, C. Bruder, R. Fazio, and G. Schön, Quantum phase transitions of interacting bosons and the supersolid phase, Phys. Rev. B **52**, 16176 (1995).

[21] P. Sengupta, L. P. Pryadko, F. Alet, M. Troyer, and G. Schmid, Supersolids Versus Phase Separation in Two-Dimensional Lattice Bosons, Phys. Rev. Lett. **94**, 207202 (2005).

[22] T. Ohgoe, T. Suzuki, and N. Kawashima, Ground-state phase diagram of the two-dimensional extended Bose-Hubbard model, Phys. Rev. B **86**, 054520 (2012).

[23] S. Wessel, Phase diagram of interacting bosons on the honeycomb lattice, Phys. Rev. B **75**, 174301 (2007).

[24] J. Y. Gan, Y. C. Wen, J. Ye, T. Li, S.-J. Yang, and Y. Yu, Extended Bose-Hubbard model on a honeycomb lattice, Phys. Rev. B **75**, 214509 (2007).

[25] T. Flottat, L. de Forges de Parny, F. Hébert, V. G. Rousseau, and G. G. Batrouni, Phase diagram of bosons in a two-dimensional optical lattice with infinite-range cavity-mediated interactions, Phys. Rev. B **95**, 144501 (2017).

[26] L. Mathey, I. Danshita, and C. W. Clark, Creating a supersolid in one-dimensional Bose mixtures, Phys. Rev. A **79**, 011602(R) (2009).

[27] G. G. Batrouni, F. Hébert, and R. T. Scalettar, Supersolid Phases in the One-Dimensional Extended Soft-Core Bosonic Hubbard Model, Phys. Rev. Lett. **97**, 087209 (2006).

[28] R. Sachdeva, M. Singh, and T. Busch, Extended Bose-Hubbard model for two-leg ladder systems in artificial magnetic fields, Phys. Rev. A **95**, 063601 (2017).

[29] K. Góral, L. Santos, and M. Lewenstein, Quantum Phases of Dipolar Bosons in Optical Lattices, Phys. Rev. Lett. **88**, 170406 (2002).

[30] V. W. Scarola and S. Das Sarma, Quantum Phases of the Extended Bose-Hubbard Hamiltonian: Possibility of a Supersolid State of Cold Atoms in Optical Lattices, Phys. Rev. Lett. **95**, 033003 (2005).

[31] S. Yi, T. Li, and C. P. Sun, Novel Quantum Phases of Dipolar Bose Gases in Optical Lattices, Phys. Rev. Lett. **98**, 260405 (2007).

[32] K.-K. Ng and Y.-C. Chen, Supersolid phases in the bosonic extended Hubbard model, Phys. Rev. B **77**, 052506 (2008).

[33] B. Capogrosso-Sansone, C. Trefzger, M. Lewenstein, P. Zoller, and G. Pupillo, Quantum Phases of Cold Polar Molecules in 2D Optical Lattices, Phys. Rev. Lett. **104**, 125301 (2010).

[34] S. Bandyopadhyay, R. Bai, S. Pal, K. Suthar, R. Nath, and D. Angom, Quantum phases of canted dipolar bosons in a two-dimensional square optical lattice, Phys. Rev. A **100**, 053623 (2019).

[35] S. Wessel and M. Troyer, Supersolid Hard-Core Bosons on the Triangular Lattice, Phys. Rev. Lett. **95**, 127205 (2005).

[36] D. Heidarian and K. Damle, Persistent Supersolid Phase of Hard-Core Bosons on the Triangular Lattice, Phys. Rev. Lett. **95**, 127206 (2005).

[37] R. G. Melko, A. Paramekanti, A. A. Burkov, A. Vishwanath, D. N. Sheng, and L. Balents, Supersolid Order from Disorder: Hard-Core Bosons on the Triangular Lattice, Phys. Rev. Lett. **95**, 127207 (2005).

[38] M. Boninsegni and N. Prokof'ev, Supersolid Phase of Hard-Core Bosons on a Triangular Lattice, Phys. Rev. Lett. **95**, 237204 (2005).

[39] A. Sen, P. Dutt, K. Damle, and R. Moessner, Variational Wave-Function Study of the Triangular Lattice Supersolid, Phys. Rev. Lett. **100**, 147204 (2008).

[40] D. Yamamoto, I. Danshita, and C. A. R. Sá de Melo, Dipolar bosons in triangular optical lattices: Quantum phase transitions and anomalous hysteresis, Phys. Rev. A **85**, 021601(R) (2012).

[41] S. V. Isakov, S. Wessel, R. G. Melko, K. Sengupta, and Y. B. Kim, Hard-Core Bosons on the Kagome Lattice: Valence-Bond Solids and Their Quantum Melting, Phys. Rev. Lett. **97**, 147202 (2006).

[42] D. Huerga, S. Capponi, J. Dukelsky, and G. Ortiz, Staircase of crystal phases of hard-core bosons on the kagome lattice, Phys. Rev. B **94**, 165124 (2016).

[43] C. Trefzger, C. Menotti, and M. Lewenstein, Pair-Supersolid Phase in a Bilayer System of Dipolar Lattice Bosons, Phys. Rev. Lett. **103**, 035304 (2009).

[44] K. Yamamoto, S. Todo, and S. Miyashita, Successive phase transitions at finite temperatures toward the supersolid state in a three-dimensional extended Bose-Hubbard model, Phys. Rev. B **79**, 094503 (2009).

[45] B. Xi, F. Ye, W. Chen, F. Zhang, and G. Su, Global phase diagram of three-dimensional extended boson Hubbard model:

A continuous-time quantum Monte Carlo study, Phys. Rev. B **84**, 054512 (2011).

[46] T. Ohgoe, T. Suzuki, and N. Kawashima, Commensurate Supersolid of Three-Dimensional Lattice Bosons, Phys. Rev. Lett. **108**, 185302 (2012).

[47] Y. Kuno, K. Shimizu, and I. Ichinose, Bosonic analogs of the fractional quantum Hall state in the vicinity of Mott states, Phys. Rev. A **95**, 013607 (2017).

[48] Y. Kuno, T. Nakafuji, and I. Ichinose, Phase diagrams of the Bose-Hubbard model and the Haldane-Bose-Hubbard model with complex hopping amplitudes, Phys. Rev. A **92**, 063630 (2015).

[49] B. Pasquiou, G. Bismut, E. Maréchal, P. Pedri, L. Vernac, O. Gorceix, and B. Laburthe-Tolra, Spin Relaxation and Band Excitation of a Dipolar Bose-Einstein Condensate in 2D Optical Lattices, Phys. Rev. Lett. **106**, 015301 (2011).

[50] S. Baier, M. J. Mark, D. Petter, K. Aikawa, L. Chomaz, Z. Cai, M. Baranov, P. Zoller, and F. Ferlaino, Extended Bose-Hubbard models with ultracold magnetic atoms, Science **352**, 201 (2016).

[51] M. Aidelsburger, M. Atala, S. Nascimbène, S. Trotzky, Y.-A. Chen, and I. Bloch, Experimental Realization of Strong Effective Magnetic Fields in an Optical Lattice, Phys. Rev. Lett. **107**, 255301 (2011).

[52] H. Miyake, G. A. Siviloglou, C. J. Kennedy, W. C. Burton, and W. Ketterle, Realizing the Harper Hamiltonian with Laser-Assisted Tunneling in Optical Lattices, Phys. Rev. Lett. **111**, 185302 (2013).

[53] M. Atala, M. Aidelsburger, M. Lohse, J. T. Barreiro, B. Paredes, and I. Bloch, Observation of chiral currents with ultracold atoms in bosonic ladders, Nature Physics **10**, 588 (2014).

[54] C. J. Kennedy, W. C. Burton, W. C. Chung, and W. Ketterle, Observation of Bose-Einstein condensation in a strong synthetic magnetic field, Nature Physics **11**, 859 (2015).

[55] D. S. Rokhsar and B. G. Kotliar, Gutzwiller projection for bosons, Phys. Rev. B **44**, 10328 (1991).

[56] W. Krauth, M. Caffarel, and J.-P. Bouchaud, Gutzwiller wave function for a model of strongly interacting bosons, Phys. Rev. B **45**, 3137 (1992).

[57] K. Sheshadri, H. R. Krishnamurthy, R. Pandit, and T. V. Ramakrishnan, Superfluid and insulating phases in an interacting-boson model: Mean-field theory and the RPA, Europhys. Lett. **22**, 257 (1993).

[58] R. Bai, S. Bandyopadhyay, S. Pal, K. Suthar, and D. Angom, Bosonic quantum Hall states in single-layer two-dimensional optical lattices, Phys. Rev. A **98**, 023606 (2018).

[59] S. Pal, R. Bai, S. Bandyopadhyay, K. Suthar, and D. Angom, Enhancement of the Bose glass phase in the presence of an artificial gauge field, Phys. Rev. A **99**, 053610 (2019).

[60] P. Buonsante, V. Penna, and A. Vezzani, Fractional-filling loop-hole insulator domains for ultracold bosons in optical superlattices, Phys. Rev. A **70**, 061603(R) (2004).

[61] D. Yamamoto, Correlated cluster mean-field theory for spin systems, Phys. Rev. B **79**, 144427 (2009).

[62] P. Pisarski, R. M. Jones, and R. J. Gooding, Application of a multisite mean-field theory to the disordered Bose-Hubbard model, Phys. Rev. A **83**, 053608 (2011).

[63] T. McIntosh, P. Pisarski, R. J. Gooding, and E. Zaremba, Multisite mean-field theory for cold bosonic atoms in optical lattices, Phys. Rev. A **86**, 013623 (2012).

[64] D.-S. Lühmann, Cluster Gutzwiller method for bosonic lattice systems, Phys. Rev. A **87**, 043619 (2013).

[65] K. W. Mahmud, E. N. Duchon, Y. Kato, N. Kawashima, R. T. Scalettar, and N. Trivedi, Finite-temperature study of bosons in a two-dimensional optical lattice, Phys. Rev. B **84**, 054302 (2011).

[66] L. de Forges de Parny, F. Hébert, V. G. Rousseau, and G. G. Batrouni, Finite temperature phase diagram of spin-1/2 bosons in two-dimensional optical lattice, Eur. Phys. J. B **85**, 169 (2012).

[67] M. Greiner, O. Mandel, T. Esslinger, T. W. Hansch, and I. Bloch, Quantum phase transition from a superfluid to a Mott insulator in a gas of ultracold atoms, Nature (London) **415**, 39 (2002).

[68] M. Iskin, Route to supersolidity for the extended Bose-Hubbard model, Phys. Rev. A **83**, 051606(R) (2011).

[69] M. Iskin, Artificial gauge fields for the Bose-Hubbard model on a checkerboard superlattice and extended Bose-Hubbard model, Eur. Phys. J. B **85**, 76 (2012).

[70] G. G. Batrouni, R. T. Scalettar, G. T. Zimanyi, and A. P. Kampf, Supersolids in the Bose-Hubbard Hamiltonian, Phys. Rev. Lett. **74**, 2527 (1995).

[71] O. Boada, A. Celi, J. I. Latorre, and V Picó, Simulation of gauge transformations on systems of ultracold atoms, New J. Phys. **12**, 113055 (2010).

[72] G. Möller and N. R. Cooper, Condensed ground states of frustrated Bose-Hubbard models, Phys. Rev. A **82**, 063625 (2010).

[73] D. Yamamoto, A. Masaki, and I. Danshita, Quantum phases of hardcore bosons with long-range interactions on a square lattice, Phys. Rev. B **86**, 054516 (2012).

[74] C. Trefzger, C. Menotti, and M. Lewenstein, Ultracold dipolar gas in an optical lattice: The fate of metastable states, Phys. Rev. A **78**, 043604 (2008).

[75] J. Werner, A. Griesmaier, S. Hensler, J. Stuhler, T. Pfau, A. Simoni, and E. Tiesinga, Observation of Feshbach Resonances in an Ultracold Gas of ^{52}Cr, Phys. Rev. Lett. **94**, 183201 (2005).

[76] A. Frisch, M. Mark, K. Aikawa, F. Ferlaino, J. L. Bohn, C. Makrides, A. Petrov, and S. Kotochigova, Quantum chaos in ultracold collisions of gas-phase erbium atoms, Nature (London) **507**, 475 (2014).

[77] T. Maier, I. Ferrier-Barbut, H. Kadau, M. Schmitt, M. Wenzel, C. Wink, T. Pfau, K. Jachymski, and P. S. Julienne, Broad universal Feshbach resonances in the chaotic spectrum of dysprosium atoms, Phys. Rev. A **92**, 060702(R) (2015).

[78] E. Lucioni, L. Tanzi, A. Fregosi, J. Catani, S. Gozzini, M. Inguscio, A. Fioretti, C. Gabbanini, and G. Modugno, Dysprosium dipolar Bose-Einstein condensate with broad Feshbach resonances, Phys. Rev. A **97**, 060701(R) (2018).